Cutoff extension of high harmonics via resonant electron injection channels

Ning Sun,[1] Xiaosong Zhu,[1,*] Liang Li,[1] Pengfei Lan,[1,†] and Peixiang Lu [1,2]

[1]*Wuhan National Laboratory for Optoelectronics and School of Physics,*
Huazhong University of Science and Technology, Wuhan 430074, China

[2]*Hubei Key Laboratory of Optical Information and Pattern Recognition, Wuhan Institute of Technology, Wuhan 430205, China*

We investigate the manipulation of electron dynamics in high-order harmonic generation from semiconductor via resonant electron injection channels, which are formed by adding ultraviolet light to the midinfrared driving laser. In the presence of these channels, valence electrons far from the top of the valence band can be first preaccelerated to the channels and then effectively injected into the conduction band, leading to a dramatic extension of the cutoff of high harmonics even with a small vector potential of the driving field. The role of the channels in the electron dynamics is unambiguously demonstrated from the time-frequency analysis and time-dependent population imaging. By adjusting the frequency of the ultraviolet field, the harmonic cutoff can be tuned in a wide range. Besides, as compared to trivial semiconductors, one can achieve the cutoff extension with a lower frequency of the ultraviolet light for topological semiconductors owing to the emergences of extra energy levels in the middle of the band gap.

I. INTRODUCTION

High-order harmonic generation (HHG) is a highly nonlinear process that up-converts intense infrared laser into the extreme ultraviolet (XUV) and soft x-ray radiation [1–3]. The harmonic radiation contains rich information about the target and has been widely employed to study the microscopic structures and ultrafast dynamics in gases [4–9] with high spatial and temporal resolutions. To date, there has been growing interest in experimental observations of HHG from solids [10–16], extending the target media from gases to condensed-matter systems [17–24]. HHG from solids is considered as a competitive alternative for obtaining the tabletop XUV light source [25] due to the low driving laser intensity and potential for high conversion efficiency originating from the high density of the bulk crystals. Moreover, solid-state HHG inspires new spectroscopy techniques that enable one to study fundamental properties and ultrafast strong light-matter interaction processes in materials. For example, high-order harmonic spectroscopy in solids constitutes a powerful tool for retrieving the energy-band structures [19,26], probing crystalline symmetries [27,28], measuring Berry curvatures [15], detecting topological phase transitions [29,30], etc.

The HHG in solids are usually considered to originate from two distinct contributions: the intraband current and the interband current [12,31,32]. The intraband current refers to the current caused by laser-driven Bloch oscillations in the individual band and the interband current results from the transitions between the valence band (VB) and conduction bands (CB). It is suggested that the high-order harmonics whose photon energy is larger than the band gap are predominantly contributed by the interband current for midinfrared (MIR) driving pulses [33,34], while the intraband HHG becomes dominant when the driving wavelength is extended toward the terahertz regime [34]. In analogy to HHG from gases, the process of interband HHG is often described with the reciprocal space trajectory picture [35,36]: Electrons in the VB are promoted to CB, continue oscillating in the driving field, and finally recombine with associated holes in the VB with emission of the high harmonics. According to this picture, for the interband harmonics, the primary plateau originates from the transitions from the first CB to the VB and the other plateaus are due to transitions from higher lying CB [37]. The cutoff [38] is determined by the highest energy difference between the CB and VB that the promoted electrons can reach in the reciprocal space. Since the electrons are promoted via tunneling in MIR fields, where the tunnel rate significantly decreases with the increase of energy gap and decrease of the electric field [39], only electrons that are preaccelerated [36] to the top of VB in the instant of the maximum electric field can be efficiently promoted and contribute HHG. Thus, the cutoff is restricted by the vector potential of the driving MIR field. A direct way to increase the cutoff is to increase the vector potential, but the intensity grows quadratically and may easily exceed the damage threshold.

Recently, the sensitivity of HHG to the spectral composition of the driving pulses has been examined theoretically and experimentally for solid targets exposed to two- or three-color laser pulses. In these investigations, the different roles of the driver electric field and corresponding vector potential are exploited and serve as a guide for increasing the harmonic yield or cutoff frequency. For example, the calculations of Song *et al.* [40] for $\omega_0 + 3\omega_0$ two-color and $\omega_0 + 3\omega_0 + 5\omega_0$ three-color pulses predict an intensity enhancement in the primary

---

*zhuxiaosong@hust.edu.cn
†pengfeilan@hust.edu.cn

plateau spectral domain and confirm the importance of preacceleration of the electrons in the VB for allowing a large range of initial crystal momenta to contribute to interband HHG. Similarly, the two-color fields can select the short or long quantum path effectively by controlling the relative phase, so that the yield at the plateau or cutoff region of the harmonic spectra can be enhanced by around one order of magnitude by adding a weak third harmonic to the fundamental field [41]. Shirai *et al.* [42] demonstrate that carrier-envelope-phase controlled subcycle MIR pulses generated through two-color filamentation have been applied for HHG in a crystalline silicon (Si) membrane experimentally, where harmonic spectrum reaches the UV region ($\leqslant 300$ nm), beyond the direct band gap of Si. The numerical calculations from Navarrete *et al.* [43] demonstrate that tuning the shape of a bichromatic driving field, by variation of the fundamental versus second-order harmonic pulse amplitude ratio and delay, can significantly enhance harmonic yields and modify the harmonic cutoff frequency. Furthermore, one can reliably extract useful information including retrieving the band structure [41] and probing electron dynamics in solids [27,44,45] from twocolor schemes. By adding a weak perturbative second-order harmonic field modulating the internal dynamics to the fundamental field, Uzan *et al.* [44] observe enhanced constructive interference in the vicinity of singularities and resolve the link between the dynamical joint density of states and the harmonic spectrum. Vampa *et al.* [45] show that, when high harmonics are detected from the input surface of a magnesium oxide crystal, a bichromatic probing of the XUV emission shows a clear synchronization largely consistent with a semiclassical model of electron-hole recollisions in bulk solids. Besides, one can observe broken inversion symmetry in solids using two-color high-order harmonic spectroscopy [27].

In this work, we consider modifying the electron dynamics in HHG from semiconductors by introducing additional promotion channels, termed resonant electron injection channels (REIC). REIC are formed by adding ultraviolet (UV) light to the MIR driving field so that electrons far from the tunnel channel can be efficiently injected into the CB via resonant excitation. In this circumstance, the cutoff of HHG is not restricted by the vector potential of the driving field and is dramatically extended. The position of the REIC in the reciprocal space can be adjusted by tuning the frequency of the UV light, and consequently the cutoff of HHG can be continuously tuned. The scheme is theoretically demonstrated with a onedimensional (1D) Su-Schrieffer-Heeger (SSH) model [46,47], which not only allows one to model trivial semiconductors but also topological semiconductors. As compared to the trivial semiconductors, one can achieve the cutoff extension with a lower frequency of the UV light in the topological semiconductors because of the emergences of extra energy levels in the middle of the band gap [48,49]. The role of the REIC in the modified electron dynamics is unambiguously revealed from the time-dependent population imaging (TDPI) and the time-frequency analysis of HHG.

II. THEORETICAL MODEL

The SSH model has been widely used in various researches for semiconductors [46,47,49], photonic crystals

[50], phononic crystals [51,52], circuits [53], etc. Recently, it has been employed to study HHG from a one-dimensional semiconductor [49]. For an even number of sites N, the SSH model consists of $N/2$ primitive cells. The atomic-site positions x_j have the form in the Cartesian coordinates [49]

$$x_j = \left(j - \frac{N+1}{2}\right)a - (-1)^j \delta, \quad j = 1, 2, \ldots, N. \quad (1)$$

Here, j is the atomic-site index. a is the separation of adjacent atoms for an equidistant distribution, i.e., $\delta = 0$. δ describes the alternating shift of the atoms causing the dimerization. Atomic units (a.u.) are used throughout this paper. The field-free electronic SSH Hamiltonian matrix is as follows:

$$\mathbf{H}_0 = \begin{pmatrix} 0 & v & & & & & \\ v & 0 & w & & & & \\ & w & 0 & v & & & \\ & & v & 0 & w & & \\ & & & \ddots & \ddots & \ddots & \\ & & & & w & 0 & v \\ & & & & & v & 0 \end{pmatrix}. \quad (2)$$

v, w are real-valued hopping elements describing the intracell hopping (between $j = 2m - 1$ and $2m$, $m = 1, \ldots, N/2$) and intercell hopping (between $j = 2m$ and $2m + 1$, $m = 1, \ldots, N/2 - 1$) of an electron respectively, which scale exponentially with the distances between neighboring sites:

$$v = -\exp[-(x_2 - x_1)] = -\exp[-(a - 2\delta)], \quad (3)$$

$$w = -\exp[-(x_3 - x_2)] = -\exp[-(a + 2\delta)]. \quad (4)$$

For $\delta > 0$ ($\delta < 0$), the system is a trivial semiconductor (topological semiconductor) [48,49,54]. $\delta = 0$ corresponds to a metal phase.

The eigenstates of the SSH Hamiltonian (2) are obtained by diagonalization. This Hamiltonian has N eigenstates,

$$\Psi_i = \left(c_i^1, c_i^2, \ldots, c_i^j, \ldots, c_i^N\right)^\top, \quad (5)$$

with $i = 0, 1, \ldots, N - 1$, where c_i^j is the value of the electronic wave function at site $j = 1, 2, \ldots, N$. As described in more detail in Ref. [55], the system consists of two bands if $\delta \neq 0$. For one electron per site, the lower band (VB) is fully populated while the upper band (CB) is empty.

The chain is coupled to linearly polarized (LP) laser fields and parallel to the laser polarization direction. The $N/2$ lowest energy states (occupied by N electrons, assuming spin degeneracy) are propagated in time in the external laser field following the time-dependent Schrödinger equation $i\frac{d}{dt}\Psi_i(t) = \mathbf{H}(t)\Psi_i(t)$. In the length gauge, the time-dependent Hamiltonian matrix reads

$$\mathbf{H}(t) = \begin{pmatrix} E(t)x_1 & v & & & \\ v & E(t)x_2 & w & & \\ & w & E(t)x_3 & v & \\ & & & \ddots & \\ & & & v & E(t)x_n \end{pmatrix}, \quad (6)$$

where $E(t) = -\partial_t A(t)$ is the electric field of the laser with the vector potential $A(t)$. Wave functions are propagated using the
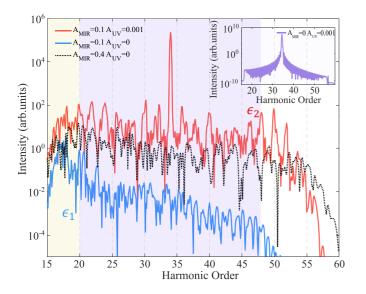
FIG. 1. The harmonic spectra in the cases of $A_{\mathrm{MIR}} = 0.1$ a.u., $A_{\mathrm{UV}} = 0.001$ a.u.; $A_{\mathrm{MIR}} = 0.1$ a.u., $A_{\mathrm{UV}} = 0$; and $A_{\mathrm{MIR}} = 0.4$ a.u., $A_{\mathrm{UV}} = 0$. The harmonic spectra have been shifted vertically for comparison. The harmonic spectrum in the case with pure UV light (see the violet solid line) is presented in the inset.

Crank-Nicolson approximation to the time-evolution operator

$$\exp[-i\mathbf{H}(t)\Delta t] = \frac{1 - i\mathbf{H}(t)\Delta t/2}{1 + i\mathbf{H}(t)\Delta t/2} + O(\Delta t^3), \qquad (7)$$

where $\Delta t = 0.1$ a.u. is the time step in our simulations. The position expectation value equals the dipole and reads

$$X(t) = \sum_{i=0}^{N/2-1} \sum_{j=1}^{N} c_i^{j*}(t) x_j c_i^j(t), \qquad (8)$$

where i labels the state and j labels the position. $c_i^j(t)$ is the value of the time-dependent wave function $\Psi_i(t)$ at site j. The harmonic spectrum for the chain is calculated by Fourier transforming the dipole acceleration $\ddot{X}(t)$ as [56]

$$P(\omega_q) = \left| \int \ddot{X}(t)\exp(-i\omega_q t)dt \right|^2 \qquad (9)$$

with $\omega_q = \frac{2q\pi}{T_0}$, $q = 1, 2, \ldots$, and T_0 the optical cycle of the fundamental driving field.

III. RESULTS AND DISCUSSION

A. Cutoff extension of HHG due to the resonant electron injection channel

We consider a chain with $N = 200$ sites, $a = 2$ a.u., and $\delta = 0.15$ a.u. This is a trivial direct-band semiconductor with band gap $\mathcal{E}_g = 0.16$ a.u., and the maximum energy difference between the CB and VB is about 0.6 a.u. (see Fig. 2). Generally, a monochromatic MIR laser field is applied to generate high harmonics. Here, we consider a laser pulse with the wavelength $\lambda_{\mathrm{MIR}} = 8.6 \times 10^4$ a.u. = 4560 nm, the amplitude of the electric field $E_{\mathrm{UV}} = 0.001$ a.u. = 0.0514 V/Å, and the intensity $I_{\mathrm{MIR}} = 3.5 \times 10^{10}$ W/cm². The vector
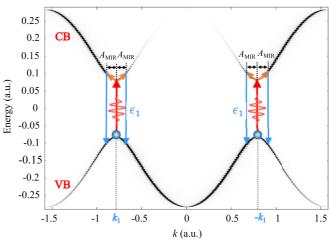

FIG. 2. Illustration of electron dynamics with only MIR driving field. The electrons are promoted via tunnel channels.

potential of the MIR pulse is given by

$$A(t) = f(t)A_{\mathrm{MIR}}\sin(\omega_{\mathrm{MIR}}t), \qquad (10)$$

with amplitude $A_{\mathrm{MIR}} = 0.1$ a.u. and frequency $\omega_{\mathrm{MIR}} = 0.01$ a.u. A sin-squared envelope $f(t) = \sin^2(\frac{\pi t}{T})$ is used to characterize the pulse profile, with the width of the driving pulse $T = 10T_0$. In our numerical calculations, the number of sites N and time step dt were tested for convergence. The calculated harmonic spectrum is shown as the blue solid line in Fig. 1. The primary plateau is denoted by the yellow-filled region. One can see that the cutoff frequency is quite low up to only the 20th order and the harmonics beyond the cutoff frequency are not clearly identified. To extend the cutoff, we add an assistant UV component to the MIR component. The wavelength of the UV light is $\lambda_{\mathrm{UV}} = 2.5 \times 10^3$ a.u. = 134 nm, the amplitude of the electric field is $E_{\mathrm{UV}} = 0.00034$ a.u. = 0.0175 V/Å, and the intensity is $I_{\mathrm{UV}} = 4.06 \times 10^9$ W/cm². The UV pulse is weaker than the MIR pulse and the peak electric field of the combined pulse reaches approximately 0.00134 a.u., which does not increase much compared to that of the MIR driver in order not to damage the sample. The vector potential field is

$$A(t) = f(t)[A_{\mathrm{MIR}}\sin(\omega_{\mathrm{MIR}}t) + A_{\mathrm{UV}}\sin(\omega_{\mathrm{UV}}t)], \qquad (11)$$

where $A_{\mathrm{UV}} = 0.001$ a.u. and $\omega_{\mathrm{UV}} = 0.34$ a.u. are the amplitude and frequency of the UV field. The calculated harmonic spectrum is presented by the red solid line in Fig. 1. The cutoff with the UV field is extended to the 48th order, as shown by the violet-filled region. The signal-to-noise ratio in the plateau is much higher and therefore the harmonics can be more clearly defined. One can see a bright peak at the 34th harmonic order corresponding to the frequency of the UV pulse.

A clear physical picture that helps us understand the cutoff extension can be obtained with the trajectory perspective on HHG, as illustrated in Figs. 2 and 3. The band structures are calculated from the Fourier transform of the eigenstates from position to k space [48,49]. For a given electron in the VB with initial crystal momentum k_0, it oscillates in the VB when
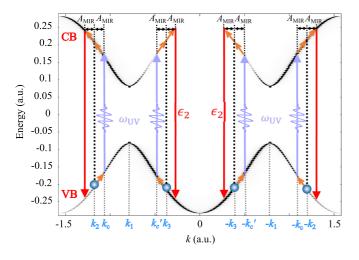
FIG. 3. Illustration of electron dynamics with the UV field ($\omega_{UV} = 0.34$ a.u.). The electrons are promoted via REIC.

the driving field is switched on until it reaches a promotion channel where electrons can be efficiently excited to the CB. This process is called preacceleration [36]. After promotion via the promotion channel, the electron continues oscillating periodically in the CB driven by the external field. Simultaneously, the occurrence of the vertical transition of the electron from the CB back to the VB leads to the harmonic radiation. The cutoff energy of HHG is determined by the maximum energy difference between CB and VB the promoted electron can reach in the reciprocal space, i.e.,

$$\max[\mathcal{E}_{CB}(k(t)) - \mathcal{E}_{VB}(k(t))], \quad (12)$$

with $\mathcal{E}_{CB}$ and $\mathcal{E}_{VB}$ being the band dispersion relations of the CB and VB and $k(t)$ being the instantaneous crystal momentum of the electron. The oscillation of the laser-driven electron in the VB and CB satisfies the acceleration theorem

$$k(t) = k_0 + A(t). \quad (13)$$

In the case with only the MIR laser field, electrons are promoted from the VB to the CB via tunneling. The tunneling rate decreases dramatically with the increase of energy difference between the two bands and the decrease of the electric field strength [39]. Therefore, the promotion channels are only available at the tops of the VB, denoted by $\pm k_1$ in Fig. 2, and efficient promotion occurs when an electron is preaccelerated at the tunnel channels in the instant of the maximum electric field. Note that the vector potential $A(t)$ is near zero when the electric field reaches its peaks in a linearly polarized field. Thus, only electrons with initial crystal momentum close to $\pm k_1$ can be excited to the CB and contribute HHG. This is why the Γ-point-only single-active-election model [37,57–59] is successfully used in many of the previous theoretical studies for linear driving fields. As shown in Fig. 2, the electron with initial crystal momentum k_1 tunnels into the CB as indicated by the solid red arrow (the preacceleration process is not shown here). Then, the laser-driven periodic oscillation of the electron in the CB (represented by solid orange arrows) is restricted in the region of $k \in [k_1 - A_{MIR}, k_1 + A_{MIR}]$. During the oscillation, the electron recombines to the VB from the

CB, generating high harmonics. The vertical transitions with largest energy difference are presented by the solid blue arrows. From this, the cutoff energy predicted in Fig. 2 is

$$\epsilon_1 = \mathcal{E}_{CB}(\pm k_1 \mp A_{MIR}) - \mathcal{E}_{VB}(\pm k_1 \mp A_{MIR}). \quad (14)$$

Considering the symmetry of the energy bands,

$$\epsilon_1 = \mathcal{E}_{CB}(k_1 + A_{MIR}) - \mathcal{E}_{VB}(k_1 + A_{MIR}). \quad (15)$$

The cutoff energy ϵ_1 predicted by Eq. (15) from the k-space semiclassical picture is consistent with the numerical result in Fig. 1.

As for the case with the UV field, apart from the tunnel channels, REIC are formed at $\pm k_c$ and $\pm k_c'$ (see the violet arrows in Fig. 3), where the difference between $\mathcal{E}_{CB}(k_c)$ and $\mathcal{E}_{VB}(k_c)$ matches the frequency of the UV light ω_{UV}. Any electron which can be preaccelerated to the positions of these channels can be promoted to the CB by absorbing a photon with frequency ω_{UV}. Note that the resonant excitation by the UV light is not sensitive to the instantaneous electric field of the MIR driving laser. Therefore, the farthest electron that can be efficiently injected into the CB are those with initial momenta $\pm k_c \mp A_{MIR}$ (i.e., $\pm k_2$) or $\pm k_c' \pm A_{MIR}$ (i.e., $\pm k_3$). Taking the initial crystal momentum k_2 for example, as shown in Fig. 3, the electron first reaches k_c during the preacceleration process (represented by the solid orange arrow). Then, the electron is injected into the CB via the REIC as indicated by the solid violet arrow. In the CB, the electron periodically oscillates in the region of $k \in [k_2 - A_{MIR}, k_2 + A_{MIR}]$ (represented by the solid orange arrows) and the occurrence of the vertical transition generates high harmonics. The transition responsible for the harmonic cutoff is represented by the solid red arrow. From this picture, the cutoff energy with UV field is

$$\epsilon_2 = \mathcal{E}_{CB}(k_c - 2A_{MIR}) - \mathcal{E}_{VB}(k_c - 2A_{MIR}), \quad (16)$$

which agrees with the numerical result in Fig. 1.

Our work reveals that the presence of REIC significantly modifies the electron dynamics so that electrons far from the tops of the VB can be injected into the CB and efficiently contribute HHG. This leads to a dramatic extension of the cutoff. Note that a very weak UV light is enough to lead to the REIC effect based on single-photon resonance. Therefore, one can choose the UV light with much lower intensity to get similar results and effectively expand the cutoff region. In order to achieve the same effect of cutoff extension by simply increasing the vector potential of the MIR driving field, the intensity will be increased by 16 times (the resultant harmonic spectrum is shown in Fig. 1 as the dashed black line). The harmonic spectrum with pure UV light is presented in the inset in Fig. 1. One can see that the radiation exists only near the resonance peak. In contrast, in the combined pulse, since the MIR field drives the injected electrons via REIC in a wide range in the CB, coherent radiation with a broad spectral range is obtained, supporting UV pulses with short duration in the time domain. The HHG process can be alternatively viewed as a frequency broadening around ω_{UV} in the presence of the MIR light.

Another interesting phenomenon in Fig. 1 is that even harmonics dominate in the plateau for the combined driving pulse
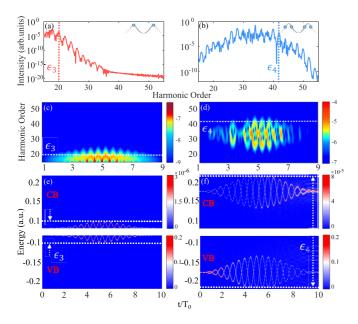
FIG. 4. Comparison of the cases without (left column) and with (right column) the UV field considering only electrons with typical initial crystal momenta. [(a), (b)] The harmonic spectra without and with the UV field. [(c), (d)] The time-frequency analysis of the HHG without and with the UV field. [(e), (f)] The TDPI and the semiclassical trajectories in the reciprocal space without and with the UV field.

(see the solid red line). Due to the conservation of energy, the harmonic frequency is given by $\Omega_{(n_{MIR}, n_{UV})} = n_{MIR}\omega_{MIR} + n_{UV}\omega_{UV}$, where n_{MIR} and n_{UV} are integer numbers denoting the numbers of driver photons absorbed (or emitted) at angular frequencies ω_{MIR} and ω_{UV}, respectively. Parity conservation requires that $n_{MIR} + n_{UV}$ is odd [60,61]. The harmonics in the plateau are contributed from the electrons that undergo injection by absorbing one UV photon, the acceleration driven by the MIR light, and the recombination in sequence, so the $(\frac{\omega_{UV}}{\omega_{MIR}} \pm 2n)$th-order harmonics dominate in the plateau, where n is an integer. Therefore, in the case of $\omega_{UV} = 0.34$ a.u., the $(34 \pm 2n)$th-order harmonics, i.e., the even harmonics, dominate in the plateau.

All the electrons in the VB are involved in the above calculations. To have a deeper insight into the results, we focus on the electrons with typical initial crystal momenta. For the case with only the MIR field, we consider the electrons at the tops of the VB, i.e., at the position of the tunnel channels. Figure 4(a) shows the obtained harmonic spectrum from these electrons. The harmonic cutoff indicated by the dashed red line is the 20th order and the cutoff energy is 0.2 a.u. As a contrast, we consider the electrons initially at $\pm k_c$ and $\pm k'_c$ (i.e., at the position of the REIC) in the case with the UV field. The obtained harmonic spectrum from these electrons is shown in Fig. 4(b). One can see that the harmonic cutoff in the latter case is much higher as compared to that in the former case. To reveal the underlying electron dynamics for the two harmonic radiation, Figs. 4(c) and 4(d) show the time-frequency analysis for Figs. 4(a) and 4(b) respectively with the Gabor transform [62]. The color maps of Figs. 4(c) and 4(d) represent the time-frequency distribution of the harmonic

intensity in the logarithmic scale. Considering the dipole acceleration $\ddot{X}(t)$, the Gabor transform (GT) is performed as

$$\mathrm{GT}(\Omega, t_0) = \frac{1}{2\pi} \int dt \, \ddot{X}(t) e^{-i\Omega t} e^{-(t-t_0)^2/2\sigma^2}, \quad (17)$$

where Ω is the frequency of the HHG. In our study, we use $\sigma = \frac{1}{4}\omega_{MIR}$. The time-frequency distribution is obtained by

$$I_{GT}(\Omega, t_0) = |\mathrm{GT}(\Omega, t_0)|^2. \quad (18)$$

As is shown in many studies, the time-dependent distribution of HHG well depicts the Bloch oscillation of the contributing electron [37,63,64]. One can see in Fig. 4(c) that the distribution oscillates forth and back periodically in the spectral range a little higher than the band gap $\mathcal{E}_g$, up to the 20th order. This is because the harmonic radiation is contributed by the electron oscillations close to the tops of the VB, as expected in Fig. 2. As for the case with the UV field, one can see that the time-frequency distribution for the harmonic radiation mainly oscillates around the 34th order and reaches up to the 42th order (represented by the horizontal dashed white line), i.e., the cutoff shown in Fig. 4(b). This time-frequency distribution well corresponds to the electron dynamical oscillations at the crystal momenta far from the tops of VB, as discussed in Fig. 3.

Another useful tool to uncover the real-time dynamics in the quantum mechanical evolution in HHG is the TDPI of electrons [65]. We first calculate the instantaneous population $|C_n(t)|^2$ on eigenstate Ψ_n by calculating the modulus square of projection of the time-dependent wave function $\Psi_i(t)$ on Ψ_n as

$$|C_n(t)|^2 = |\langle \Psi_n | \Psi_i(t) \rangle|^2 \quad (19)$$

with $n = 0, 1, \ldots, N - 1$. The TDPI is obtained by plotting $|C_n(t)|^2$ as a function of time t and eigenenergy $\mathcal{E}_n$ of the Hamiltonian H_0, as shown in Figs. 4(e) and 4(f), corresponding to the HHG in Figs. 2(a) and 2(b) respectively. One can see clear energy-resolved population oscillations of electrons in the respective bands in the TDPI. These population oscillations correspond to the Bloch oscillations of electrons in reciprocal space, where the electrons are driven forth and back periodically by the external laser field. The semiclassical trajectories in the reciprocal space according to Eq. (13) are also presented in Figs. 4(e) and 4(f) by the thin dashed white lines. One can see that the semiclassical trajectories agree well with the profiles of the TDPI from the quantum mechanical simulations. Again, Fig. 4(e) indicates that the electrons oscillate close to the band gap, which attributes to the excitations via the tunnel channels. The maximum energy difference between the population in the CB and VB is up to ϵ_3 (see the horizontal thick dashed lines), which agrees with the cutoff energy in Fig. 4(a). As for the case with the UV field shown in Fig. 4(f), the population oscillates far from the band gap, i.e., the electrons in the VB never pass through the tunnel channels. Meanwhile, the population in the VB becomes smaller over time while the population in the CB becomes larger, indicating an efficient injection via the REIC. Consequently, the maximum energy difference is up to a much larger value ϵ_4 (see the horizontal thick dashed lines), which agrees with the cutoff energy in Fig. 4(b).
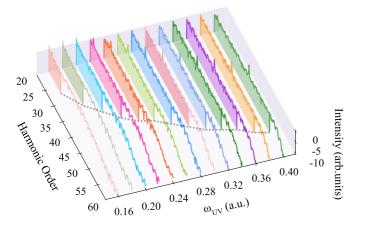
FIG. 5. The harmonic spectra in the cases of ω_{UV} varying from 0.16 to 0.40 a.u. with a step of 0.2 a.u.

Based on the above discussions, by adjusting the frequency of the UV field, one can adjust the position of the REIC so that the cutoff of the HHG can be tuned in a wide range. As is demonstrated in Fig. 5, we calculate the harmonic spectra and identify their cutoff (denoted by filled regions with different colors) in the cases of ω_{UV} varying from 0.16 to 0.40 a.u. with a step of 0.2 a.u. One can see the cutoff is continuously tuned from the 27th order to the 52th order.

B. Cutoff extension of HHG in topological semiconductors

Apart from the electron injection and control of electron dynamics in trivial semiconductors, we also discuss those in topological semiconductors. Here, we change $\delta = 0.15$ a.u. to $\delta = -0.15$ a.u. The band structure of the chain is shown in Fig. 6(a), where the band gap $\mathcal{E}_g = 0.16$ a.u. More importantly, the chain transits from a trivial phase to a topological phase. Two topological edge states emerge with nearly zero energy in the middle of the band gap [48,49]. These edge states are spatially highly localized at the edges of the chain and therefore widely spread in the k space. Due to the emergences of the edge states, electrons can be injected into the CB in two steps: first to the edge state by absorbing one photon and then to the CB by absorbing another photon. The REIC locate where the energy difference between the two bands is twice of the UV photon energy, denoted by k_c and k_c'. Similarly, any electron that can be preaccelerated to the position of REIC can be injected into the CB and efficiently contribute HHG. The dynamics of the electrons responsible for the harmonic cutoff (with initial crystal momenta $\pm k_4$ and $\pm k_5$) are illustrated in Fig. 6(a). The maximum reachable energy difference ϵ_5 satisfies

$$\epsilon_5 = \mathcal{E}_{\mathrm{CB}}(k_c - 2A_{\mathrm{MIR}}) - \mathcal{E}_{\mathrm{VB}}(k_c - 2A_{\mathrm{MIR}}) \qquad (20)$$

and is much larger than that for electrons promoted via the tunnel channels at the tops of the VB. The numerical results are shown in Fig. 6(b). Since the REIC can be formed in a two-step manner, the required wavelength of the assistant field can be longer. Here, we consider $\omega_{\mathrm{UV}} = 0.16$ a.u. corresponding to the wavelength $\lambda_{\mathrm{UV}} = 5.4 \times 10^3$ a.u. $= 285$ nm. The other laser parameters remain the same. The harmonic
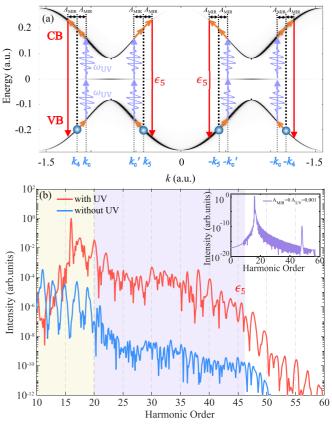

FIG. 6. (a) Illustration of the electron dynamics with the UV field ($\omega_{\mathrm{UV}} = 0.16$ a.u.) in the topological semiconductor. (b) The harmonic spectra with and without the UV field in the topological semiconductor. The harmonic spectrum in the case with pure UV light (see the violet solid line) is presented in the inset.

spectra in the cases with and without the UV field are shown as the red and blue lines, with the primary plateaus indicated by the violet-filled and yellow-filled regions respectively. The harmonic cutoff with the UV field is the 47th order and agrees with ϵ_5 predicted by Eq. (20), while the harmonic cutoff with only the MIR field is the 20th order. The cutoff is significantly extended by adding the UV light. The harmonic spectrum with pure UV light is presented in the inset in Fig. 6. One can see that the radiation only exists near ω_{UV} and $3\omega_{\mathrm{UV}}$. In contrast, in the combined pulse, the MIR field drives the injected electrons via REIC in a wide range in the CB, contributing to coherent radiation with a broad spectral range. Thus, one can achieve the frequency broadening of the UV light in the presence of the MIR light.

IV. CONCLUSION

In summary, we show that, by introducing new injection channels called REIC with assistant UV light, the electron dynamics in HHG from semiconductors are dramatically modified. Unlike typical HHG dynamics where only electrons at the tops of VB can be efficiently promoted to the CB via tunneling, electrons far away from the tops of the VB can be effectively injected into the CB via REIC. As a result, the cutoff of HHG is not restricted by the vector potential of the driving field and is dramatically extended. The cutoff region

can also be tuned in a wide range by adjusting the position of the REIC with the different frequency of the UV light. In the presence of topological edge states, the REIC can be formed with a two-step excitation so that the cutoff extension can take place with a lower frequency of the UV light. The role of the REIC in the manipulation of the electron dynamics is revealed with the time-frequency analysis and TDPI.

Although we demonstrate our scheme with a one-dimensional SSH chain as a prototype, the effect of the REIC is general and not restricted to the SSH chain. The valence electrons far from the top of VB can be efficiently injected into CB via REIC based on the resonant excitation irrespective of the dimension or band structure of the target semiconductor. Then the injected electrons will substantially contribute to HHG with large cutoff due to the dynamics depicted in Figs. 3 and 6(a). Therefore, our proposed ideal can be used for various kinds of real materials, such as zinc oxide crystals, magnesium oxide crystals, etc. In the presence of the UV light, one can see that the excitation of electrons is dominated by the single-photon resonance. In this case, one can focus on the two energy bands coupled by the resonance. However,

it is possible that in many systems there are also higher CB coupled by the resonance. The higher bands are not included in our model. If they are considered, one would see a dramatic enhancement of the second or even higher plateaus due to the electron injection via REIC into higher CB and also harmonics of the UV light in these plateaus. This is out of the scope of this work. In this paper, we focus on the cutoff extension of the primary plateau, which can be well described by models with two bands and is not affected by the higher CB [37].

[1] P. B. Corkum and F. Krausz, Nat. Phys. **3**, 381 (2007).

[2] F. Krausz and M. Ivanov, Rev. Mod. Phys. **81**, 163 (2009).

[3] H. Niikura and P. B. Corkum, in *Attosecond and Angstrom Science*, edited by P. R. Berman, C. C. Lin and E. Arimondo, Advances in Atomic Molecular and Optical Physics 54 (Elsevier Inc., 2007), pp. 511–548.

[4] R. Kienberger, M. Hentschel, M. Uiberacker, C. Spielmann, M. Kitzler, A. Scrinzi, M. Wieland, T. Westerwalbesloh, U. Kleineberg, U. Heinzmann, M. Drescher, and F. Krausz, Science **297**, 1144 (2002).

[5] J. Itatani, J. Levesque, D. Zeidler, H. Niikura, H. Pépin, J. C. Kieffer, P. B. Corkum, and D. M. Villeneuve, Nature (London) **432**, 867 (2004).

[6] S. Baker, J. S. Robinson, C. A. Haworth, H. Teng, R. A. Smith, C. C. Chirilă, M. Lein, J. W. G. Tisch, and J. P. Marangos, Science **312**, 424 (2006).

[7] O. Smirnova, Y. Mairesse, S. Patchkovskii, N. Dudovich, D. Villeneuve, P. Corkum, and M. Y. Ivanov, Nature (London) **460**, 972 (2009).

[8] X. Zhu, M. Qin, Q. Zhang, Y. Li, Z. Xu, and P. Lu, Opt. Express **21**, 5255 (2013).

[9] P. M. Kraus, B. Mignolet, D. Baykusheva, A. Rupenyan, L. Horný, E. F. Penka, G. Grassi, O. I. Tolstikhin, J. Schneider, F. Jensen, L. B. Madsen, A. D. Bandrauk, F. Remacle, and H. J. Wörner, Science **350**, 790 (2015).

[10] S. Ghimire, A. D. DiChiara, E. Sistrunk, P. Agostini, L. F. DiMauro, and D. A. Reis, Nat. Phys. **7**, 138 (2011).

[11] B. Zaks, R. B. Liu, and M. S. Sherwin, Nature (London) **483**, 580 (2012).

[12] O. Schubert, M. Hohenleutner, F. Langer, B. Urbanek, C. Lange, U. Huttner, D. Golde, T. Meier, M. Kira, S. W. Koch, and R. Huber, Nat. Photon. **8**, 119 (2014).

[13] N. Tancogne-Dejean, O. D. Mücke, F. X. Kärtner, and A. Rubio, Nat. Commun. **8**, 1 (2017).

[14] Y. S. You, D. Reis, and S. Ghimire, Nat. Phys. **13**, 345 (2017).

[15] T. T. Luu and H. J. Wörner, Nat. Commun. **9**, 916 (2018).

[16] N. Klemke, N. Tancogne-Dejean, G. M. Rossi, Y. Yang, F. Scheiba, R. E. Mainz, G. Di Sciacca, A. Rubio, F. X. Kärtner, and O. D. Mücke, Nat. Commun. **10**, 1319 (2019).

[17] K. K. Hansen, D. Bauer, and L. B. Madsen, Phys. Rev. A **97**, 043424 (2018).

[18] C. Yu, K. K. Hansen, and L. B. Madsen, Phys. Rev. A **99**, 013435 (2019).

[19] L. Li, P. Lan, L. He, W. Cao, Q. Zhang, and P. Lu, Phys. Rev. Lett. **124**, 157403 (2020).

[20] S. Fu, Y. Feng, J. Li, S. Yue, X. Zhang, B. Hu, and H. Du, Phys. Rev. A **101**, 023402 (2020).

[21] C. Yu, H. Iravani, and L. B. Madsen, Phys. Rev. A **102**, 033105 (2020).

[22] A.-W. Zeng and X.-B. Bian, Phys. Rev. Lett. **124**, 203901 (2020).

[23] A. Flettner, T. Pfeifer, D. Walter, C. Winterfeldt, C. Spielmann, and G. Gerber, Appl. Phys. B **77**, 747 (2003).

[24] H. G. Kurz, D. S. Steingrube, D. Ristau, M. Lein, U. Morgner, and M. Kovačev, Phys. Rev. A **87**, 063811 (2013).

[25] T. T. Luu, M. Garg, S. Y. Kruchinin, A. Moulet, M. T. Hassan, and E. Goulielmakis, Nature (London) **521**, 498 (2015).

[26] G. Vampa, T. J. Hammond, N. Thiré, B. E. Schmidt, F. Légaré, C. R. McDonald, T. Brabec, D. D. Klug, and P. B. Corkum, Phys. Rev. Lett. **115**, 193603 (2015).

[27] T. T. Luu and H. J. Wörner, Phys. Rev. A **98**, 041802(R) (2018).

[28] N. Saito, P. Xia, F. Lu, T. Kanai, J. Itatani, and N. Ishii, Optica **4**, 1333 (2017).

[29] R. E. F. Silva, A. Jiménez-Galán, B. Amorim, O. Smirnova, and M. Ivanov, Nat. Photon. **13**, 849 (2019).

[30] A. Chacón, D. Kim, W. Zhu, S. P. Kelly, A. Dauphin, E. Pisanty, A. S. Maxwell, A. Picón, M. F. Ciappina, D. E. Kim, C. Ticknor, A. Saxena, and M. Lewenstein, Phys. Rev. B **102**, 134115 (2020).

[31] M. Hohenleutner, F. Langer, O. Schubert, M. Knorr, U. Huttner, S. W. Koch, M. Kira, and R. Huber, Nature (London) **523**, 572 (2015).

[32] N. Tancogne-Dejean, O. D. Mücke, F. X. Kärtner, and A. Rubio, Phys. Rev. Lett. **118**, 087403 (2017).

[33] C. R. McDonald, G. Vampa, P. B. Corkum, and T. Brabec, Phys. Rev. A **92**, 033845 (2015).

[34] G. Vampa, C. R. McDonald, G. Orlando, P. B. Corkum, and T. Brabec, Phys. Rev. B **91**, 064302 (2015).

[35] G. Vampa and T. Brabec, J. Phys. B: At., Mol. Opt. Phys. **50**, 083001 (2017).

[36] L. Li, P. Lan, X. Zhu, T. Huang, Q. Zhang, M. Lein, and P. Lu, Phys. Rev. Lett. **122**, 193901 (2019).

[37] M. Wu, S. Ghimire, D. A. Reis, K. J. Schafer, and M. B. Gaarde, Phys. Rev. A **91**, 043839 (2015).

[38] Without losing generality, we focus on the cutoff of the primary plateau, which is strongest.

[39] C. Zener and R. H. Fowler, Proc. R. Soc. London A **145**, 523 (1934).

[40] X. Song, S. Yang, R. Zuo, T. Meier, and W. Yang, Phys. Rev. A **101**, 033410 (2020).

[41] T.-J. Shao, L.-J. Lü, J.-Q. Liu, and X.-B. Bian, Phys. Rev. A **101**, 053421 (2020).

[42] H. Shirai, F. Kumaki, Y. Nomura, and T. Fuji, Opt. Lett. **43**, 2094 (2018).

[43] F. Navarrete and U. Thumm, Phys. Rev. A **102**, 063123 (2020).

[44] A. J. Uzan, G. Orenstein, A. Jiménez-Galán, C. McDonald, R. E. F. Silva, B. D. Bruner, N. D. Klimkin, V. Blanchet, T. Arusi-Parpar, M. Krüger, A. N. Rubtsov, O. Smirnova, M. Ivanov, B. Yan, T. Brabec, and N. Dudovich, Nat. Photon. **14**, 183 (2020).

[45] G. Vampa, J. Lu, Y. S. You, D. R. Baykusheva, M. Wu, H. Liu, K. J. Schafer, M. B. Gaarde, D. A. Reis, and S. Ghimire, J. Phys. B: At., Mol. Opt. Phys. **53**, 144003 (2020).

[46] W. P. Su, J. R. Schrieffer, and A. J. Heeger, Phys. Rev. Lett. **42**, 1698 (1979).

[47] A. J. Heeger, S. Kivelson, J. R. Schrieffer, and W. P. Su, Rev. Mod. Phys. **60**, 781 (1988).

[48] D. Bauer and K. K. Hansen, Phys. Rev. Lett. **120**, 177401 (2018).

[49] C. Jürß and D. Bauer, Phys. Rev. B **99**, 195428 (2019).

[50] L. J. Maczewsky, M. Heinrich, M. Kremer, S. K. Ivanov, M. Ehrhardt, F. Martinez, Y. V. Kartashov, V. V. Konotop, L. Torner, D. Bauer, and A. Szameit, Science **370**, 701 (2020).

[51] P. St-Jean, V. Goblot, E. Galopin, A. Lemaître, T. Ozawa, L. Le Gratiet, I. Sagnes, J. Bloch, and A. Amo, Nat. Photon. **11**, 651 (2017).

[52] Y. Long, J. Ren, and H. Chen, Phys. Rev. Lett. **124**, 185501 (2020).

[53] Y. Wang, L.-J. Lang, C. H. Lee, B. Zhang, and Y. D. Chong, Nat. Commun. **10**, 1102 (2019).

[54] H. Drüeke and D. Bauer, Phys. Rev. A **99**, 053402 (2019).

[55] J. K. Asbóth, L. Oroszlány, and A. Pályi, *A Short Course on Topological Insulators*, Lecture Notes in Physics (Springer, Heidelberg, 2016), Vol. 919.

[56] B. Sundaram and P. W. Milonni, Phys. Rev. A **41**, 6571 (1990).

[57] M. Wu, D. A. Browne, K. J. Schafer, and M. B. Gaarde, Phys. Rev. A **94**, 063403 (2016).

[58] Z. Guan, X.-X. Zhou, and X.-B. Bian, Phys. Rev. A **93**, 033852 (2016).

[59] J.-B. Li, X. Zhang, S.-J. Yue, H.-M. Wu, B.-T. Hu, and H.-C. Du, Opt. Express **25**, 18603 (2017).

[60] A. Fleischer, O. Kfir, T. Diskin, P. Sidorenko, and O. Cohen, Nat. Photon. **8**, 543 (2014).

[61] L. Medišauskas, J. Wragg, H. van der Hart, and M. Y. Ivanov, Phys. Rev. Lett. **115**, 153001 (2015).

[62] C. C. Chirilă, I. Dreissigacker, E. V. van der Zwan, and M. Lein, Phys. Rev. A **81**, 033412 (2010).

[63] T.-Y. Du and X.-B. Bian, Opt. Express **25**, 151 (2017).

[64] X. Zhang, J. Li, Z. Zhou, S. Yue, H. Du, L. Fu, and H.-G. Luo, Phys. Rev. B **99**, 014304 (2019).

[65] X. Liu, X. Zhu, P. Lan, X. Zhang, D. Wang, Q. Zhang, and P. Lu, Phys. Rev. A **95**, 063419 (2017).